JOURNAL OF COMPUTATIONAL PHYSICS **106**, 19–29 (1993)

Finite Volume Calculations of Self-Sustained Oscillations in a Grooved Channel

J. C. F. PEREIRA AND J. M. M. SOUSA

Instituto Superior Técnico/Technical University of Lisbon, Mechanical Engineering Department, Av. Rovisco Pais, 1096 Lisbon Codex, Portugal

Received March 2, 1992

A numerical simulation of unsteady incompressible Navier–Stokes flow in a periodically grooved channel is performed for Reynolds numbers $R \sim O(10^3)$. The numerical scheme is based on finite differences approximation with an explicit quadratic Leith-type of temporal discretization. Periodic self-sustained oscillatory flow is reported to occur in the investigated flow configuration, indicating a Hopf bifurcation. The threshold for the onset of self-sustained flow oscillations is the critical Reynolds number $950 < R_c < 1050$. The numerical predictions are in good agreement with reported spectral element method solutions, demonstrating the accuracy and efficiency of the present method.

1. INTRODUCTION

Cavity flows and flows in grooved channels present a wide variety of problems of interest to both theoretical and computational dynamicists. The most striking feature of these flows, under certain flow conditions, is their unsteadiness. Periodic self-sustained oscillations have been observed as a result of fluid-dynamic instability, fluid-resonance, or elastic displacement of solid boundaries, see, e.g., Reihman and Saberky [14], Sarohia [18], Rockwell and Naudasher [17], Rockwell and Knisely [16]. Problems of this nature may be present in a wide class of relevant engineering applications ranging from wind tunnels with slotted walls (see King *et al.* [10]), to gasdynamic lasers or the cooling of electronic components, see, e.g., Sparrow *et al.* [20].

Steady laminar cavity flows have been widely investigated and used as test cases for validating incompressible flow algorithms, see, e.g., Burggraf [2], Pan and Acrivos [13], and Ghia *et al.* [7]. However, the inherent difficulty to obtain accurate numerical solutions of unsteady Navier–Stokes flows explains the scarcity of numerical studies aiming to identify the flow mechanisms responsible for fluid-dynamic excitation and self-sustained oscillations. The physical issue is very complex due to the interaction of several coexisting mechanisms such as: leading-edge interaction, Biot–Savart induction, or upstream pressure waves (feedback condition) and the selective amplification of vorticity fluctuations in the cavity shear layer (see, e.g., Rockwell [15]). Simplified models based in shear layer considerations have been formulated aiming to predict the frequencies of the oscillations. Although these models have proved reasonable success in predicting some characteristics of the organized flow oscillations, they constitute incomplete analyses, neglecting the role of important mechanisms, such as the recirculating flow field inside the cavity and the interaction with the main flow.

In order to be able to provide a complete understanding of the aforementioned flow behavior, accurate direct numerical simulations of the full Navier–Stokes equations must be performed. Fortunately, the increase of computing power has made possible the numerical investigation of the amazing dynamical features exhibited by the unsteady Navier–Stokes equations. Fortin *et al.* [5] presented the transition from a steady solution to chaotic flow and the presence of strange attractors in a two-dimensional cascade flow. Gustafson and Halasi [9] and, more recently, Goodrich *et al.* [8] investigated the occurrence of a Hopf bifurcation in a lid driven cavity, using a high-order finite differences method. They have provided detailed information about how to extract qualitative properties from the solution of time-dependent differential equations. A similar study was performed by Shen [19], following the methodology described in [8], using a spectral method. However, a different cavity aspect ratio was considered. In the above cited work, the authors have dedicated strong efforts to show that the periodic solutions obtained were not merely artifacts of the numerical approximation. With this goal in mind, it seemed ostensibly adequate to pursue a direct comparison between solutions provided by two different numerical formulations: high-order finite differences and spectral methods. So, we refer to the work of Ghaddar *et al.* [6] who investigated the presence of self-sustained flow oscillations in periodically grooved channels, using a spectral element method. In the present work an explicit quadratic Leith-type of temporal discretization (see Leonard

0021-9991/93 $5.00

[11]) was used together with 106×84 mesh nodes. The selected grooved channel geometrical flow configuration and the Reynolds number equal to 1200 were the same as those reported in [6]. It is our purpose to continue the study of Ghaddar *et al.* [6] by further addressing the question of whether the selection of the temporal and convective discretization schemes precludes the possibility of using numerical predictions to extract substantial insight about non-linear flows. In Section 2, the solution algorithm used for the computations reported in this paper is briefly described. In Section 3, the numerical solution of a decaying Tollmien–Schlichting wave in a plane channel as well as the onset of self-sustained oscillations in a grooved channel are presented. This is followed by a detailed analysis of the grooved channel flow structure at $R = 1200$. Finally, Section 4 provides the main conclusions of the present work.

2. NUMERICAL FORMULATION

2.1. *Problem Formulation and Governing Equations*

The two-dimensional Navier–Stokes and continuity equations for an incompressible viscous fluid are

$$\frac{\partial \mathbf{v}}{\partial t} + (\mathbf{v} \cdot \nabla)\mathbf{v} = -\nabla p + \nu \nabla^2 \mathbf{v} \tag{1}$$

$$\nabla \cdot \mathbf{v} = 0 \tag{2}$$

for $\mathbf{v} = (u, v)$, where u and v are the velocity components in the x and y directions respectively, in a Cartesian reference frame, p is the ratio of pressure to constant density, ν is the kinematic viscosity, and t is time. Envisaging a finite volume formulation, Eq. (1) may be expressed in a conservative form given by

$$\phi_t + (u\phi)_x + (v\phi)_y = -p_x + \nu(\phi_{xx} + \phi_{yy}). \tag{3}$$

The flow problem for which a solution of Eqs. (1) and (2) is required is that of the periodically grooved channel flow, proposed by Ghaddar *et al.* [6] (see Fig. 1). The channel is assumed to be infinite in the extent of the streamwise x direction and the flow is taken as independent of the spanwise co-ordinate. The channel half width H and the velocity scale $\frac{3}{2}u_B$, where u_B is the cross-channel average velocity, are used to non-dimensionalize lengths and velocities, respectively.

2.2. *Discretization Schemes*

The numerical approach described by the finite-volume method is used to discretize the governing equations on a staggered grid system, as shown in Fig. 2a. An explicit quadratic Leith-type of temporal discretization was chosen because of its third-order accuracy. This scheme was proposed by Leonard [11] and it is known as the QUICKEST scheme. Very few multidimensional fluid flow problems have been predicted using this scheme (see Davies and Moore [4]), therefore a brief derivation is outlined in this section.

Equation (3) is integrated over a time increment Δt and over the control volume $\mathbf{v}$ surrounding a grid node. The first term yields

$$\int_t^{t+\Delta t} \int_{\mathbf{v}} \phi_t \, d\mathbf{v} \, dt = \int_{-\Delta y/2}^{\Delta y/2} \int_{-\Delta x/2}^{\Delta x/2} (\phi^{n+1} - \phi^n) \, d\xi \, d\eta$$
$$= \mathbf{v}(\bar{\phi}^{n+1} - \bar{\phi}^n), \tag{4}$$

where $\bar{\phi}$ stands for the mean values in the control volume. Considering, for the sake of simplicity, a uniformly spaced mesh in both co-ordinate directions and, further, assuming that the dependent variable is defined in a local reference frame (ξ, η) by a quadratic function,

$$\phi = c_1 + c_2\xi + c_3\xi^2 + c_4\eta + c_5\eta^2 + c_6\xi\eta, \tag{5}$$

the mean values $\bar{\phi}$ may be obtained as

$$\bar{\phi} = \frac{1}{\Delta x \, \Delta y} \iint \phi \, d\xi \, d\eta = c_1 + \frac{c_3}{12}\Delta x^2 + \frac{c_5}{12}\Delta y^2 \tag{6}$$

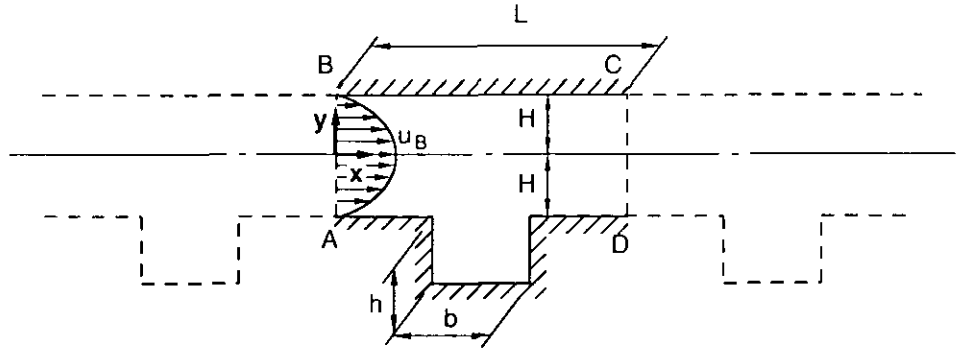

FIG. 1. Geometrical flow configuration.

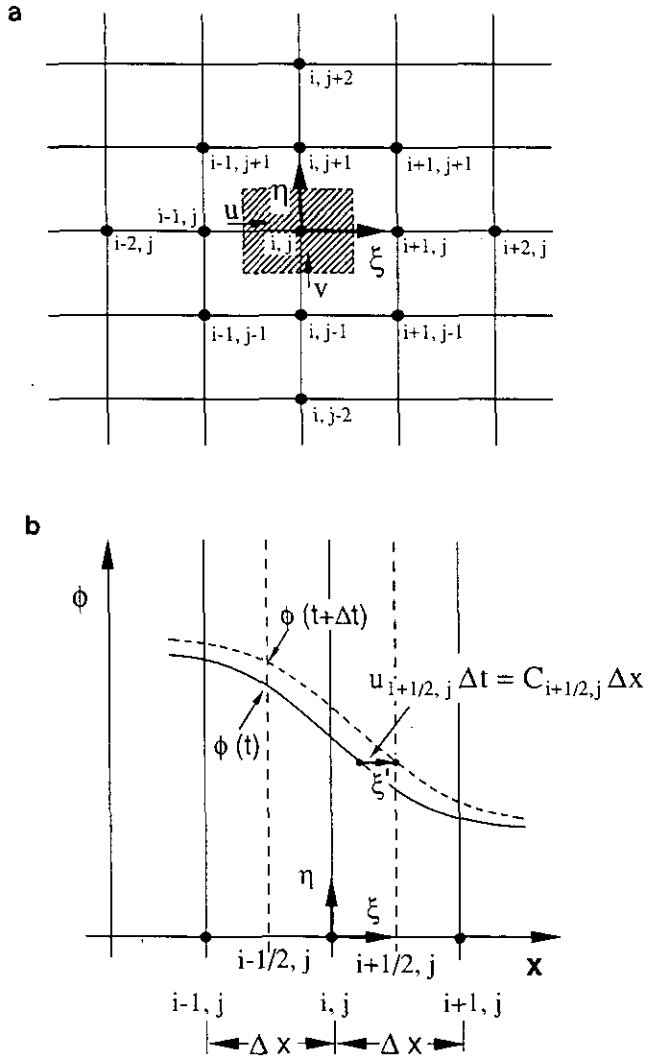

FIG. 2. (a) 13-point finite differences molecule. (b) Explicit quadratic Leith-type of interpolation.

and Eq. (4) appears as

$$\int_t^{t+\Delta t}\int_v \phi_t\, d\mathbf{v}\, dt = \mathbf{v}\left[(c_1^{n+1}-c_1^n)+\frac{\Delta x^2}{12}(c_3^{n+1}-c_3^n) + \frac{\Delta y^2}{12}(c_5^{n+1}-c_5^n)\right]. \tag{7}$$

However, $c_3=\frac{1}{2}(\partial^2\phi/\partial\xi^2)$ and $c_5=\frac{1}{2}(\partial^2\phi/\partial\eta^2)$, yielding

$$\frac{\Delta x^2}{12}(c_3^{n+1}-c_3^n)=\frac{\Delta x^2}{24}\Delta t\left[\frac{\partial}{\partial t}\left(\frac{\partial^2\phi}{\partial\xi^2}\right)\right] \tag{8a}$$

$$\frac{\Delta y^2}{12}(c_5^{n+1}-c_5^n)=\frac{\Delta y^2}{24}\Delta t\left[\frac{\partial}{\partial t}\left(\frac{\partial^2\phi}{\partial\eta^2}\right)\right]. \tag{8b}$$

The terms $(\partial/\partial t)(\partial^2\phi/\partial\xi^2)$ and $(\partial/\partial t)(\partial^2\phi/\partial\eta^2)$ may be obtained by taking the second derivative of Eq. (3) and neglecting fourth-order derivatives:

$$\frac{\partial}{\partial t}\left(\frac{\partial^2\phi}{\partial\xi^2}\right)\cong -\frac{\partial^2}{\partial\xi^2}\left[\frac{\partial(u\phi)}{\partial\xi}\right]-\frac{\partial^2}{\partial\xi^2}\left[\frac{\partial(v\phi)}{\partial\eta}\right] \cong -\frac{\partial}{\partial\xi}\left[\frac{\partial^2(u\phi)}{\partial\xi^2}\right] \tag{9a}$$

$$\frac{\partial}{\partial t}\left(\frac{\partial^2\phi}{\partial\eta^2}\right)\cong -\frac{\partial^2}{\partial\eta^2}\left[\frac{\partial(u\phi)}{\partial\xi}\right]-\frac{\partial^2}{\partial\eta^2}\left[\frac{\partial(v\phi)}{\partial\eta}\right] \cong -\frac{\partial}{\partial\eta}\left[\frac{\partial^2(v\phi)}{\partial\eta^2}\right]. \tag{9b}$$

So Eq. (8a) becomes

$$\frac{\Delta x^2}{12}(c_3^{n+1}-c_3^n) = -\frac{\Delta x}{24}\Delta t\left[\frac{\partial^2(u\phi)}{\partial\xi^2}\right]_{i-1/2,j}^{i+1/2,j} = -\frac{\Delta x}{24}\Delta t[2(c_3u)_{i+1/2,j}-2(c_3u)_{i-1/2,j}] \tag{10}$$

and we have a similar expression for Eq. (8b). Replacing c_1, c_3, and c_5 by their values, as functions of the dependent variables in the (ξ, η) referential, we obtain

$$\int_t^{t+\Delta t}\int_v \phi_t\, d\mathbf{v}\, dt = \mathbf{v}\left\{(\phi_{i,j}^{n+1}-\phi_{i,j}^n)-\left[\frac{\Delta x^2}{24}\times(C_{i+1/2,j}\,\mathrm{CURV}^+_{i+1/2,j} - C_{i-1/2,j}\,\mathrm{CURV}^+_{i-1/2,j}) + \frac{\Delta y^2}{24}(C_{i,j+1/2}\,\mathrm{CURV}^+_{i,j+1/2} - C_{i,j-1/2}\,\mathrm{CURV}^+_{i,j-1/2})\right]^n\right\}, \tag{11}$$

where $C_{i\pm1/2,j\pm1/2}$ stand for the Courant numbers, e.g., $C_{i+1/2,j}=u_{i+1/2,j}\,\Delta t/\Delta x$, and $\mathrm{CURV}^+_{i\pm1/2,j\pm1/2}$ denote finite differences approximations to a second derivative:

$$\mathrm{CURV}^+_{i+1/2,j}=(\phi_{i-1,j}+\phi_{i+1,j}-2\phi_{i,j})/\Delta x^2 \tag{12a}$$

$$\mathrm{CURV}^+_{i,j+1/2}=(\phi_{i,j-1}+\phi_{i,j+1}-2\phi_{i,j})/\Delta y^2. \tag{12b}$$

The finite-differences counterpart of the convection and diffusion terms is evaluated as

$$\int_t^{t+\Delta t}\int_v\left(\frac{\partial(u\phi)}{\partial\xi}-\nu\frac{\partial^2\phi}{\partial\xi^2}\right)d\mathbf{v}\,dt = \int_t^{t+\Delta t}\left[u\phi-\nu\frac{\partial\phi}{\partial\xi}\right]_{i-1/2,j}^{i+1/2,j}\mathscr{A}\,dt \tag{13}$$

and the first term in Eq. (13) may be written as

$$\int_t^{t+\Delta t} [u\phi]_{i-1/2,j}^{i+1/2,j} \mathscr{A}\, dt = \int_t^{t+\Delta t} [u\phi]_{i+1/2,j} \mathscr{A}\, dt - \int_t^{t+\Delta t} [u\phi]_{i-1/2,j} \mathscr{A}\, dt. \quad (14)$$

For conciseness, only the convective flux at the $(i+\frac{1}{2}, j)$ control volume face is discretized, considering $u_{i+1/2,j} > 0$; see Fig. 2b. Thus, replacing the temporal integration by Lagrangian integrals,

$$\int_t^{t+\Delta t} [u\phi]_{i+1/2,j} \mathscr{A}\, dt = \int_0^{\Delta\xi'} [\tilde{\phi}(\xi')]\, \mathscr{A}\, d\xi', \quad (15)$$

where $\Delta\xi' = \int_{t+\Delta t}^{t} u_{i+1/2,j}\, dt = C_{i+1/2,j}\, \Delta x$, and evaluating the mean value $\tilde{\phi}$ at the $(i+1/2, j)$ control volume face, $\tilde{\phi} = c_1 + c_2\xi' + c_3\xi'^2 + (c_5/12)\,\Delta y^2$, yields

$$\int_0^{\Delta\xi'} [\tilde{\phi}(\xi')]\, \mathscr{A}\, d\xi' = \mathscr{A}\left[c_1\xi' + \frac{c_2}{2}\xi'^2 + \frac{c_3}{3}\xi'^3 + \frac{c_5}{12}\Delta y^2\, \xi' \right]_{\Delta x/2 - C_{i+1/2,j}\Delta x}^{\Delta x/2}. \quad (16)$$

The coefficients c_1, c_2, c_3, and c_5 are obtained from the quadratic function (5), at time t, in the referential (ξ, η).

The convective fluxes at the remaining faces $(i-\frac{1}{2}, j)$ and $(i, j\pm\frac{1}{2})$ are discretized similarly. If $u_{i+1/2,j} < 0$, the referential (ξ, η) will be located at the $(i+1, j)$ grid node. A similar procedure is followed for the diffusion fluxes. The mean value of the diffusive unit flux at the control volume face $(i+\frac{1}{2}, j)$ is given, in the Lagrangian space, by $\partial\tilde{\phi}/\partial\xi' = c_2 + 2c_3\xi'$, leading to:

$$\int_t^{t+\Delta t} \left[\nu \frac{\partial\tilde{\phi}}{\partial\tilde{\xi}} \right]_{i+1/2,j} \mathscr{A}\, dt = \int_0^{\Delta\xi'} \frac{\nu}{u_{i+1/2,j}} \frac{\partial\tilde{\phi}}{\partial\xi'}\, \mathscr{A}\, d\xi' = \left[\frac{\nu}{u_{i+1/2,j}} (c_2\xi' + c_3\xi'^2) \right]_{\Delta x/2 - C_{i+1/2,j}\Delta x}^{\Delta x/2}. \quad (17)$$

The explicit finite differences are obtained by rearranging the resulting finite differences expressions from Eqs. (16) and (17), adding Eq. (11) and the explicit counterpart of source terms. Thus, the dependent variable at the $(n+1)$ time step, for each control volume, is obtained from

$$\phi_{i,j}^{n+1} = \phi_{i,j}^{n} + (F_{i-1/2,j} - F_{i+1/2,j} + F_{i,j-1/2} - F_{i,j+1/2} + R_{i,j} + S_{i,j})^n, \quad (18)$$

where the fluxes, say, e.g., $F_{i+1/2,j}$, are given by $F_{i+1/2,j} = \Psi_1 + \Psi_2 + \Psi_3$:

$$\Psi_1 = \mathscr{A} C_{i+1/2,j}\, \Delta x \left[\left(\frac{\phi_{i+1,j} + \phi_{i,j}}{2} \right) - C_{i+1/2,j} \left(\frac{\phi_{i+1,j} - \phi_{i,j}}{2} \right) \right] \quad (19a)$$

$$\Psi_2 = \mathscr{A}\, dx \left[-\frac{\Delta x^2}{6} (1 - C_{i+1/2,j}^2 - 3\gamma) \times (\alpha\, \mathrm{CURV}_{i+1/2,j}^{+} + \beta\, \mathrm{CURV}_{i+1/2,j}^{-}) + \frac{\Delta y^2}{24} (\alpha\, \mathrm{CURV}_{i,j+1/2}^{+} + \beta\, \mathrm{CURV}_{i,j+1/2}^{-}) \right] \quad (19b)$$

$$\Psi_3 = -\mathscr{A}\gamma\, \Delta x \left[(\phi_{i+1,j} - \phi_{i,j}) - \frac{\Delta x^2}{2} \times (\alpha\, \mathrm{CURV}_{i+1/2,j}^{+} + \beta\, \mathrm{CURV}_{i+1/2,j}^{-}) \right], \quad (19c)$$

where $\alpha = (C_{i+1/2,j} + |C_{i+1/2,j}|)/2$, $\beta = (C_{i+1/2,j} - |C_{i+1/2,j}|)/2$, and $\gamma = \nu\, \Delta t/\Delta x^2$. The control volume face area is represented by $\mathscr{A}$ and

$$\mathrm{CURV}_{i+1/2,j}^{-} = (\phi_{i,j} + \phi_{i+2,j} - 2\phi_{i+1,j})/\Delta x^2 \quad (20a)$$

$$\mathrm{CURV}_{i,j+1/2}^{-} = (\phi_{i+1,j+1} + \phi_{i+1,j-1} - 2\phi_{i+1,j})/\Delta y^2. \quad (20b)$$

Finally, the pressure gradient term is given by

$$R_{ij} = \nu \frac{\Delta t}{\Delta x} (p_{i-1,j} - p_{i,j}) \quad (21)$$

and $S_{i,j}$ are the additional source terms.

The velocity divergence for a control volume is driven approximately to zero by adjusting the control volume pressure. The pressure adjustment produces a corresponding velocity adjustment, which for the u-velocity component is determined, e.g., for $u_{i+1/2,j}$, by

$$u'_{i+1/2,j} = \frac{\Delta t}{\rho} \frac{(p'_{i,j} - p'_{i+1,j})}{\Delta x} \quad (22)$$

for $u = u^* + u'$ and $p = p^* + p'$.

The integration of the continuity equation and its discretization using the corrected velocity field $\mathbf{v} = \mathbf{v}^* + \mathbf{v}'$ yields the finite differences equation for the pressure correction, resulting in the system of algebraic equations

$$[A]\{p'\} = \{M\}, \quad (23)$$

where $[A]$ is the coefficients matrix and $\{M\}$ denotes the out-of-balance mass source terms in each control volume.

The system of equations is solved iteratively, using the strong implicit method, see Stone [21] and Azevedo *et al.* [1].

A von Neumann stability analysis was conducted by Leonard [11] for the one-dimensional finite differences equation, showing a considerable improvement over other explicit methods, namely a significant stable region in the range $1 \leqslant C \leqslant 2$ for finite γ. However, due to accuracy requirements, all calculations were performed for $C < 1$.

2.3. *Numerical Algorithm and Boundary Conditions*

For each time step the calculations start with the explicit solution of the streamwise and normal momentum equations, allowing the calculation of u^* and v^* at each control volume. This is followed by the iterative solution of the pressure correction equation (23), updating the velocity and pressure fields, $\mathbf{v} = \mathbf{v}^* + \mathbf{v}'$ and $p = p^* + p'$.

The boundary conditions (see Fig. 1) for the velocity $\mathbf{v}$ are

$$\mathbf{v}(x, y, t) = 0, \qquad \text{on} \quad \overline{AD} \text{ and } \overline{BC},$$
$$\mathbf{v}(x + L, y, t) = \mathbf{v}(x, y, t), \qquad \text{on} \quad \overline{AB} \text{ and } \overline{CD},$$

while for the pressure we impose that

$$p(x, y, t) = -\beta(t)x + p'(x, y, t)$$
$$p'(x + L, y, t) = p'(x, y, t), \qquad \text{on} \quad \overline{AB} \text{ and } \overline{CD},$$

where $\beta(t)$ is the driving force for the flow.

3. RESULTS

3.1. *Plane Poiseuille Flow*

A strong interaction between plane channel and shear layer instabilities is expected to occur in the periodically grooved channel flow under consideration. As stated by Ghaddar *et al.* [6], the occurring instability process involves the interaction of a shear layer and a Tollmien–Schlichting wave. Therefore, accurate solution of the plane Poiseuille problem is a minimum requirement for any numerical scheme purporting to simulate the full grooved channel flow.

The grooved channel geometry reduces to plane channel flow in the limit $h \to 0$, see Fig. 1. The linear stability analysis of plane channel flow with respect to infinitesimal disturbances of the harmonic form,

$$\mathbf{v}'(x, y, t) = \mathscr{R}e\left[\hat{\mathbf{v}}(y) \exp i(\alpha x - 2\pi\omega_L t)\right] \exp(\sigma_L t), \qquad (24)$$

leads to a linear ordinary fourth-order differential equation for the amplitude function $\hat{\mathbf{v}}(y)$, known as the Orr–Sommerfeld equation. The solution of this equation, coupled with the appropriate boundary conditions for $\hat{\mathbf{v}}(y)$, yields a characteristic equation,

$$\mathscr{L}(\omega_L, \sigma_L, \alpha, R) = 0, \qquad (25)$$

connecting the frequency ω_L, the amplification (or damping) rate σ_L, and the wavenumber α, defining an eigenvalue problem, where R stands for the Reynolds number.

Our first goal is to test the performance of the present algorithm by direct simulation of the full Navier–Stokes equations. So, we will consider the direct simulation of Eqs. (1) and (2), using as an initial condition the exact eigenfunction for the least stable Orr–Sommerfeld mode given by (25), superimposed to the basic laminar flow $u_b = (1 - y^2)$. The solution of (25) was obtained using the semi-implicit finite differences method proposed by Cebeci and Keller [3], yielding a stable mode with $\alpha = 0.9424$, $\omega_L = 0.0503$, and $\sigma_L = -0.0459$, for $R = 1000$ (see Fig. 3a).

The mesh used for the Navier–Stokes predictions comprised 62×53 control volumes, overlapping a computational domain of length $L = 6.666$ and height $2H$. The time step was $\Delta t = 0.004$, yielding a maximum Courant number $C \approx 0.05$ in the solution domain. Figure 3b shows the perturbation streamlines at $t = \tau/2 = 1/(2\omega_L)$. There is virtually no change in the shape of the travelling wave, indicating an accurate solution with low numerical dispersion. According to Orszag [12], the plane Poiseuille flow is stable to small disturbances for $R \leqslant 5772$. In fact, the predicted perturbation amplitude is seen to decay in time, as shown in Fig. 4 for the v-velocity component at $(x, y) = (3.333, 0)$, exhibiting a frequency $\omega = 0.050$ and an amplification (damping) rate $\sigma = -0.044$. These values are in very good agreement with both solutions obtained from the Orr–Sommerfeld equation and from the direct simulation of a

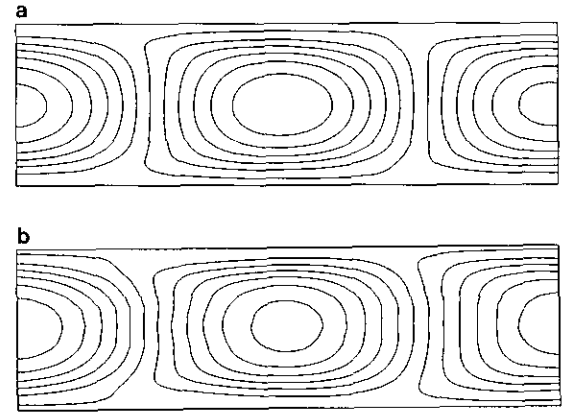

FIG. 3. Perturbation streamlines for plane channel flow, at $R = 1000$: (a) Obtained from the solution of the Orr–Sommerfeld equation, at $t = 0$. (b) Obtained by direct simulation of the Navier–Stokes equations, at $t = \tau/2$.

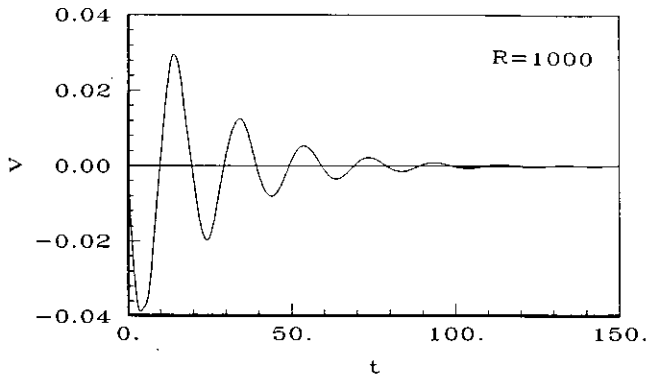

FIG. 4. v-velocity component at $(x, y) = (3.333, 0)$ as a function of time, obtained by direct simulation of the plane channel flow at $R = 1000$.

linearized form of the Navier–Stokes equations presented by Ghaddar *et al.* [6]. The present calculations suggest that our numerical algorithm is accurate enough to describe convective instability of hydrodynamic nature.

3.2. *Grooved Channel. Onset of Periodic Oscillations*

In this section we carry out numerical calculations of the full Navier–Stokes equations, for the geometry depicted in Fig. 1, aiming to predict the critical Reynolds number R_c, corresponding to the onset of self-sustained oscillations in the grooved channel. The geometrical parameters describing the computational domain correspond to $h = 1.111$, $b = 2.222$, and $L = 6.666$. The periodic flow yields a wavenumber $\alpha = 1.885$, corresponding to a two-wave system. A mesh comprising 106×84 control volumes was used in these computations, and the time step was chosen in order to keep a low Courant number $C \approx 0.2$. Figure 5 shows the parameters ω and σ obtained from direct simulation of the full Navier–Stokes equations for ascending Reynolds numbers. These values reveal, once again, good agreement with linear theory results presented in [6].

As the Reynolds number is further increased, the numerical solution approaches a time asymptotic behavior, displaying finite amplitude oscillations. In order to show the onset of these oscillations we have plotted, in Fig. 6, the v-velocity component at $(x, y) = (3.179, -0.967)$ as a function of time for various Reynolds numbers in the vicinity of R_c. From these results one can qualitatively estimate that the critical Reynolds number is approximately $950 < R_c < 1050$. A more precise determination of R_c is proposed in the next paragraphs.

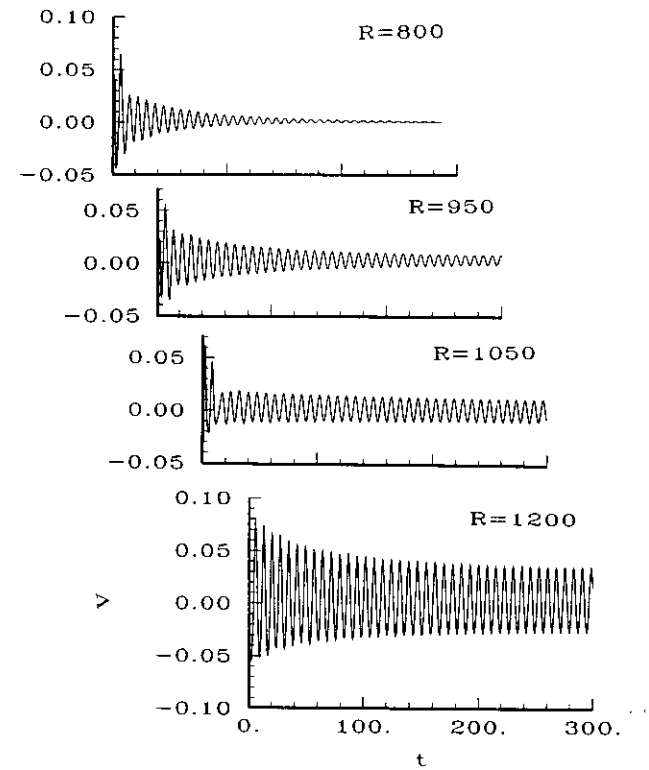

FIG. 6. v-velocity component at $(x, y) = (3.179, -0.967)$ as a function of time, obtained by direct simulation of the grooved channel flow for subcritical and supercritical Reynolds numbers R.

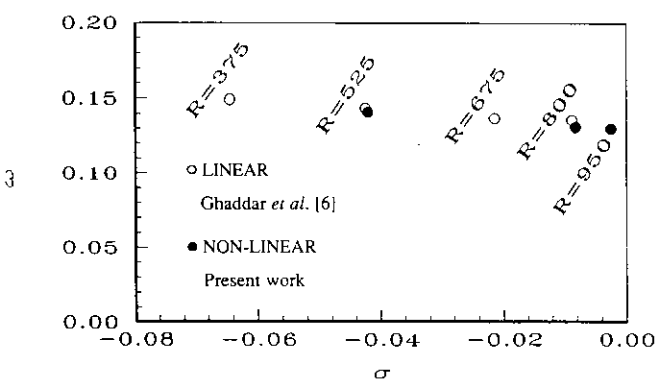

FIG. 5. Stability diagram for the subcritical grooved channel flow, parametrized by the Reynolds number R.

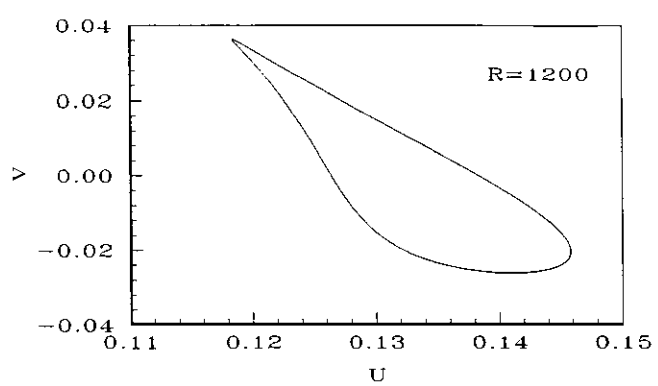

FIG. 7. Phase plane portrait of v vs. u in the grooved channel at $(x, y) = (3.179, -0.967)$, for the Reynolds number $R = 1200$.

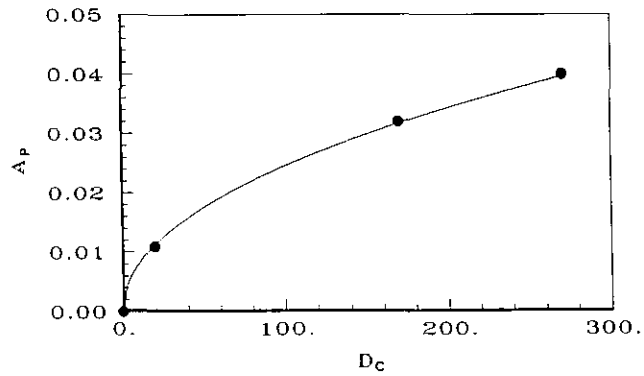

FIG. 8. Amplitude of self-sustained oscillations at $(x, y) = (3.179, -0.967)$, as a function of degree of criticality D_c.

The periodic time asymptotic behavior of the supercritical flow at $R = 1200$ is confirmed by the cyclic trajectory drawn in the phase space (see Fig. 7), denoting a periodic attractor. The frequency of the limit cycles is independent of the degree of criticality $D_c = (R - R_c)$ within the investigated range. Table I lists the computed frequencies for various supercritical flow Reynolds numbers. The predicted parameters follow the tendency indicated by the subcritical flow simulations.

Ghaddar *et al.* [6] found a square-root dependency between the oscillations amplitude and D_c. This behavior is

TABLE I

Computed Frequencies for Various Supercritical Flow Reynolds Numbers R

R	ω
1050	0.131
1200	0.132
1300	0.132

associated with a regular Hopf bifurcation. A pointwise amplitude parameter $A_p = \max_t |\overline{v_p} - v_p|$, where an overbar denotes a time-averaged quantity, was evaluated from the predictions for each Reynolds number investigated. A least-squares fit on $\ln(A_p) = a_1 \ln(D_c) + a_2$ was also performed for the different Reynolds numbers, as shown in Fig. 8. Assuming $R_c = 1030$, the results yielded $a_1 = 0.48437$ and $a_2 = -5.93939$ with the best correlation coefficient $r = 0.99999$. These values suggest that the onset of self-sustained oscillations occur at $R_c = 1030$. A slightly different procedure was followed in [6]. They have estimated $R_c = 975$ from the behavior of the oscillations amplitude levels. For $R_c = 975$ the parameter a_1 became equal to $a_1 = 0.48275$ with a correlation coefficient $r = 0.99961$. Unfortunately it was not possible to compare the oscillations amplitude levels predicted by the two methods, since

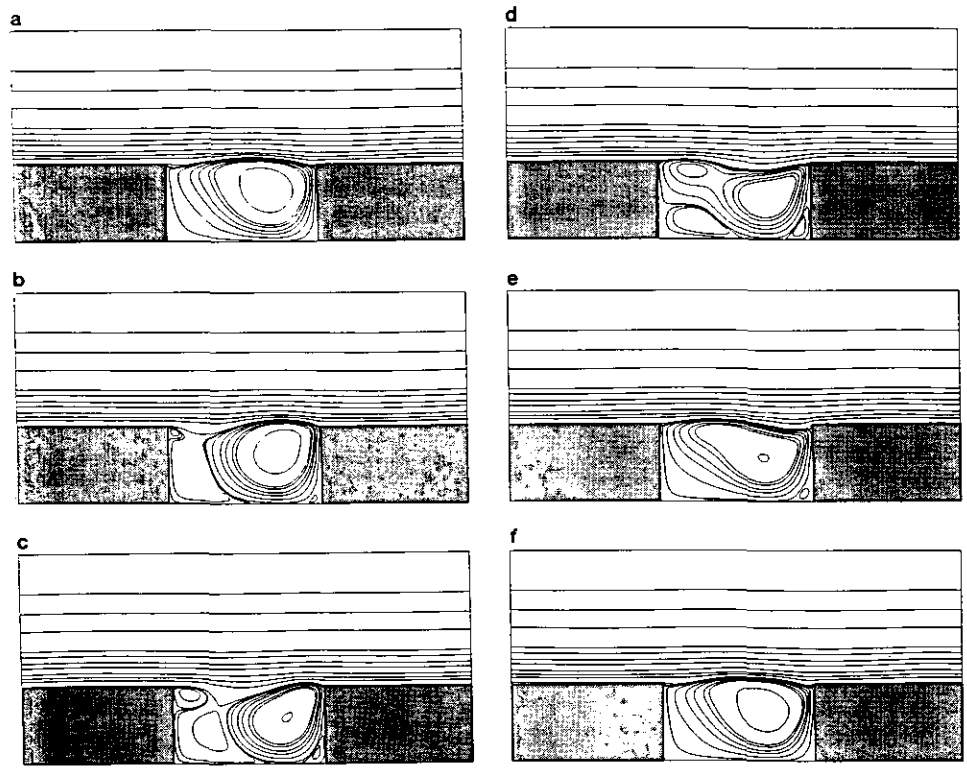

FIG. 9. Portraits of flow streamlines during a complete time cycle, at $R = 1200$: (a) $t = 0$; (b) $t = \tau/5$; (c) $t = 2\tau/5$; (d) $t = 3\tau/5$; (e) $t = 4\tau/5$; (f) $t = \tau$.

the location of the monitor point was not given. The observed difference between the predicted values of R_c should be attributed to the adopted strategy to estimate the onset of self-sustained oscillations rather than to numerical discrepancies. The accuracy of the above results is therefore comparable with spectral solutions.

It is well known that grid spacing and time increments are influencing parameters on solution accuracy; see, e.g., Goodrich *et al.* [8]. For $R = 1200$ several tests were conducted in order to evaluate the effectiveness of the numerical scheme. The calculations were performed using three different computational meshes, keeping a maximum Courant number of approximately $C \approx 0.2$, aiming to select the optimum grid for further computations. The selected grids comprised 53×42, 106×84, and 120×92 control volumes. The predictions obtained with the coarser grid left unanswered the question of whether a stable state displaying finite amplitude periodic oscillations or a steady solution exists, for $R = 1200$. The amplitude of the self-sustained oscillations, after attaining an apparent stable state, was slightly damped with time although the frequency of the oscillations remained equal to $\omega = 0.135$. The results obtained using 106×84 control volumes clearly show that an asymptotic state has been reached and that this asymptotic state is indeed periodic. Power spectral analysis of the instantaneous velocity components over a large number of cycles provided the information on the oscillation frequency $\omega = 0.132$. Calculations over a few cycles, obtained using the finer computational grid comprising 120×92 control volumes, denoted that the oscillation frequency was in fact equal to $\omega = 0.132$. Furthermore, the time increment was halved, yielding a maximum Courant number $C \approx 0.1$. The frequency of the oscillations remained equal to $\omega = 0.132$, indicating that the numerical solution is not affected by any further change in time or grid refinements.

3.3. *Grooved Channel. Flow Structure*

Detailed predictions of the flow for $R = 1200$ will be presented in this section for comparison with spectral solutions [6] and also to provide the flow structure and the mechanics of well-established self-sustained oscillations.

Dynamical characteristics will be discussed in terms of instantaneous streamlines, perturbation streamlines, pressure and vorticity contours, during a complete time cycle. Figure 9 shows the flow streamlines displaying the dynamics of the recirculation eddies. Starting at the instant when the primary vortex occupies the whole cavity, at $t = \tau/5$ a secondary vortex is seen to be ejected from the separation edge. Then, this vortex grows by the entrainment of fluid promoted on the shear layer and travels downstream ($t = 3\tau/5$). For $t = 4\tau/5$, the coalescence of the

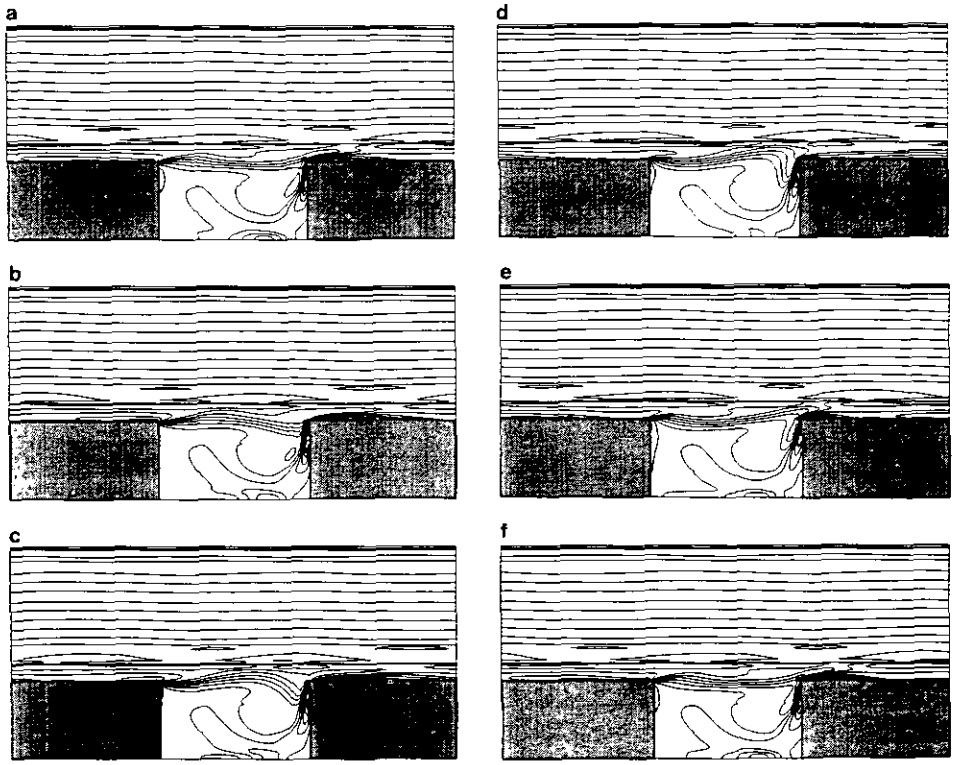

FIG. 10. Portraits of vorticity contours during a complete time cycle, at $R = 1200$: (a) $t = 0$; (b) $t = \tau/5$; (c) $t = 2\tau/5$; (d) $t = 3\tau/5$; (e) $t = 4\tau/5$; (f) $t = \tau$.

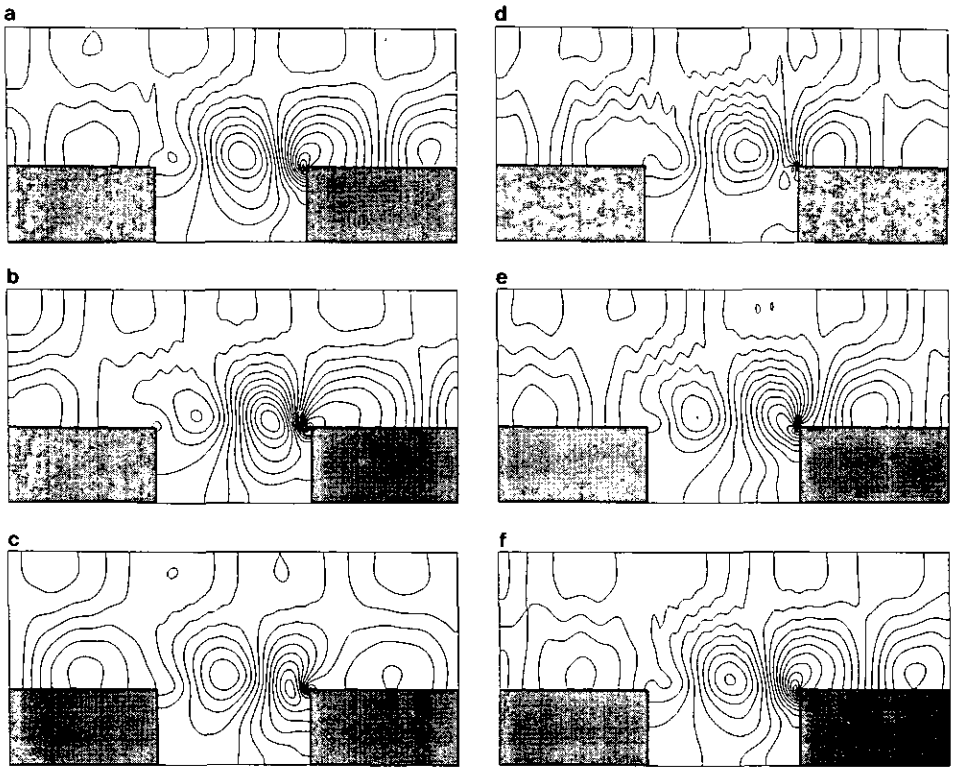

FIG. 11. Portraits of pressure contours during a complete time cycle, at $R = 1200$: (a) $t = 0$; (b) $t = \tau/5$; (c) $t = 2\tau/5$; (d) $t = 3\tau/5$; (e) $t = 4\tau/5$; (f) $t = \tau$.

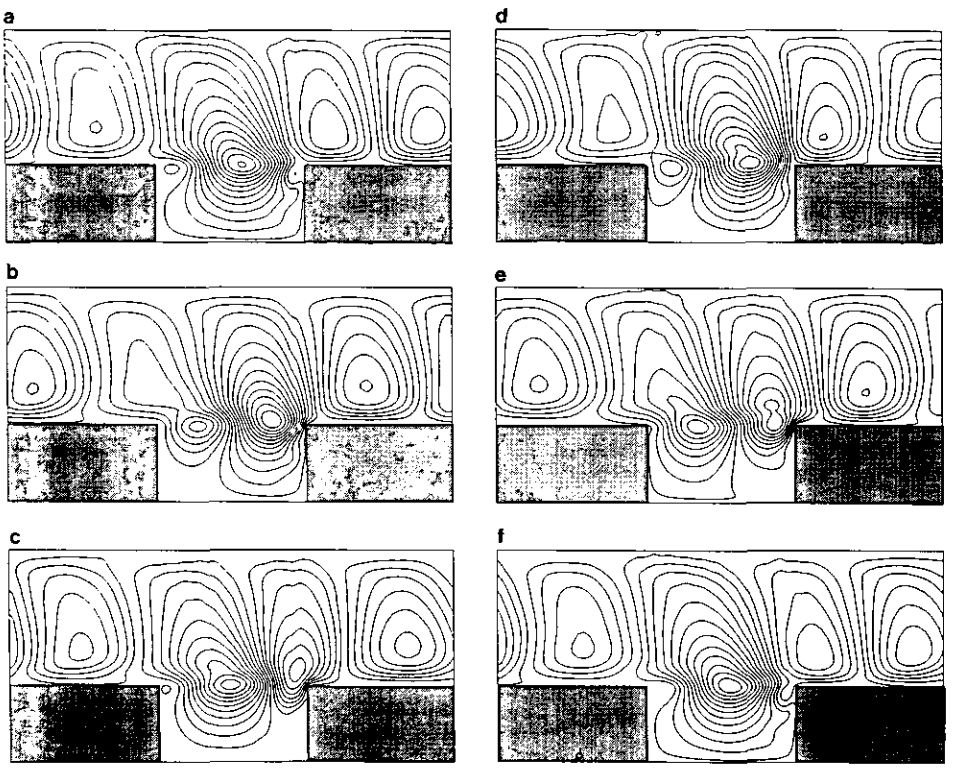

FIG. 12. Portraits of perturbation streamlines during a complete time cycle, at $R = 1200$: (a) $t = 0$; (b) $t = \tau/5$; (c) $t = 2\tau/5$; (d) $t = 3\tau/5$; (e) $t = 4\tau/5$; (f) $t = \tau$.

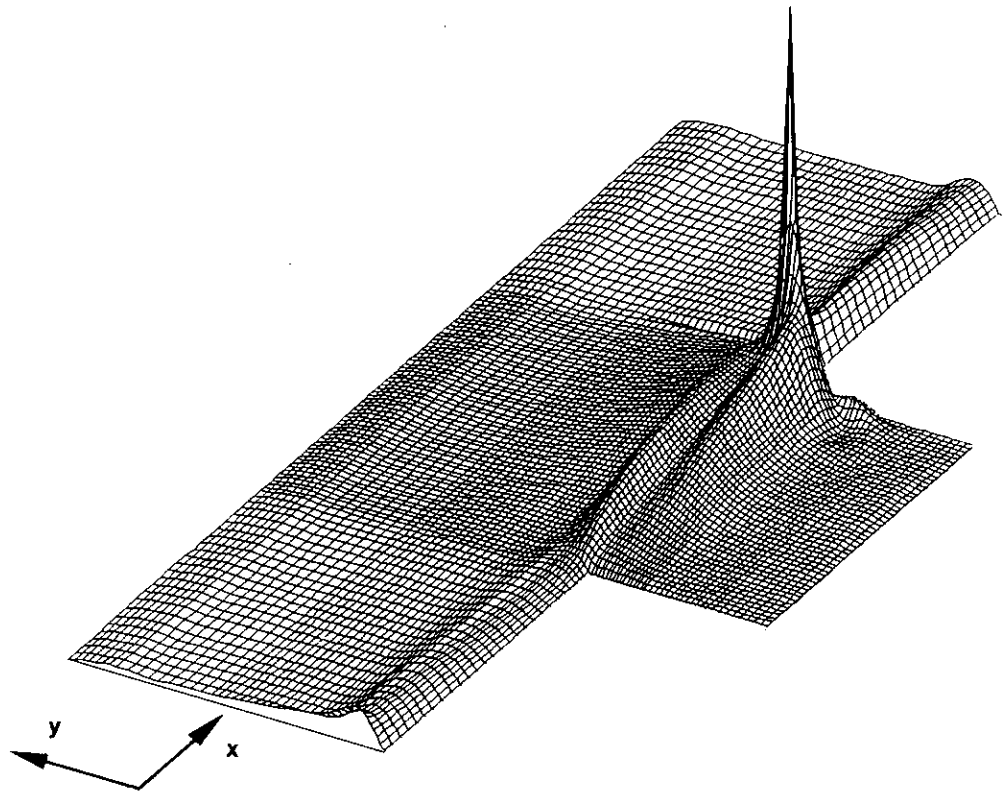

FIG. 13. Time-averaged perturbation kinetic energy surface plot, at $R = 1200$.

secondary vortex with the main vortex is seen to occur. The motion of the primary vortex strongly suggests that the process proceeds leading to vortex shedding ($t = 3\tau/5$ to $t = 4\tau/5$). These observations are distinctly corroborated by Fig. 10, where vortex shedding, on the downstream edge, is clearly observed from $t = 3\tau/5$ to $t = 4\tau/5$. A certain amount of vorticity is therefore, periodically shed, travelling downstream. Vortex rollup is also noticeable being, in conjunction with the pressure signature on the cavity edge (see Fig. 11), an indubitable indication of the flapping behavior associated with Kelvin–Helmholtz instability.

Another feature of the flow under consideration may be enhanced by plotting the perturbation streamlines, as shown in Fig. 12. These sequential portraits reveal the presence of a travelling wave in the grooved channel, driven by the above mentioned vortex shedding, which is in accordance to previous work [6]. The remarkable resemblance to a Tollmien–Schlichting wave (cf. Fig. 3) seems to indicate that this kind of instability, characteristic of plane channel flow, is still present in the grooved channel, although somehow modified due to the need of adaptation to a more complex geometry. The vortical structures are now clearly seen to travel over the cavity, impinging on the downstream edge.

Figure 13 shows the perturbation kinetic energy surface plot obtained by time-averaged instantaneous velocity fluctuations $\frac{1}{2}(\overline{u'^2} + \overline{v'^2})$. The figure highlights the role of the shear layer and the dramatic effect of the presence of the downstream groove corner, providing further amplification of the enhanced coherent disturbances.

4. CONCLUSIONS

A direct numerical simulation of incompressible moderate Reynolds number flow in a periodically grooved channel was performed, using finite difference formulation, together with an explicit quadratic Leith-type of temporal discretization. The problem of the decaying of a Tollmien–Schlichting wave in a plane channel, for a Reynolds number $R = 1000$, was previously considered in order to investigate the effectiveness of the numerical scheme.

The presented flow solutions have been carefully compared with spectral element predictions of the same flow problem and later used in a qualitative study of the properties exhibited by the dynamical system under consideration. The main conclusions of the present work may be summarized as follows:

(a) The finite differences method outlined in this work have demonstrated robustness and comparable accuracy to

spectral element method solutions, for direct numerical simulation of $R \sim O(10^3)$ flows;

(b) For the investigated grooved channel flow, transition from a steady state to a stable oscillatory regime is seen to occur at a critical Reynolds number of approximately $950 < R_c < 1050$. Moreover, the good agreement between the present predictions and spectral solutions should be ample proof that the periodic *self-sustained* oscillatory flow is not a consequence of numerical artifacts.

ACKNOWLEDGMENT

The authors gratefully acknowledge FCCN—Fundação para o Cálculo Cientifico Nacional—for computing facilities.

REFERENCES

1. J. L. T. Azevedo, F. Durst, and J. C. F. Pereira, *Appl. Math. Model.* **12**, 51 (1988).
2. O. Burgraff, *J. Fluid Mech.* **24**, 113 (1966).
3. T. Cebeci and H. B. Keller, AGARD CP 224, Paper 7, 1977 (unpublished).
4. R. W. Davis and E. F. Moore, *J. Fluid Mech.* **116**, 475 (1982).
5. A. Fortin, M. Fortin, and J. J. Gervais, *J. Comput. Phys.* **70**, 295 (1987).
6. N. K. Ghaddar, K. Z. Korczak, B. B. Mikic, and A. T. Patera, *J. Fluid Mech.* **163**, 99 (1986).
7. U. Ghia, K. N. Ghia, and C. T. Shin, *J. Comput. Phys.* **48**, 387 (1982).
8. J. W. Goodrich, K. Gustafson, and K. Halasi, *J. Comput. Phys.* **90**, 219 (1990).
9. K. Gustafson and K. Halasi, *J. Comput. Phys.* **70**, 271 (1987).
10. J. L. King, P. Boyle, and J. B. Ogle, *J. Fluid Mech.* **4**, 283 (1958).
11. B. P. Leonard, *Methods Appl. Mech. Eng.* **19**, 89 (1979).
12. S. A. Orszag, *J. Fluid Mech.* **50**, 689 (1971).
13. F. Pan and A. Acrivos, *J. Fluid Mech.* **28**, 643 (1967).
14. T. C. Reihman and R. H. Saberky, *Int. J. Heat Mass Transfer* **11**, 1083 (1968).
15. D. Rockwell, *AIAA J.* **21**, 645 (1983).
16. D. Rockwell and C. Knisely, *J. Fluid Mech.* **93**, 413 (1979).
17. D. Rockwell and E. Naudasher, *ASME J. Fluids Eng.* **100**, 152 (1978).
18. V. Sarohia, *AIAA J.* **15**, 984 (1977).
19. J. Shen, *J. Comput. Phys.* **95**, 228 (1991).
20. E. M. Sparrow, S. B. Vemuri, and D. S. Kadle, *Int. J. Heat Mass Transfer* **26**, 689 (1983).
21. H. L. Stone, *SIAM J. Numer. Anal.* **5**, 530 (1968).